Chapter II

Synthesis, characterization and growth mechanism of Gd_2O_3 nanosystems

2.1 Principle and characterization techniques employed

Synthesis of nanomaterial is a topic of intensive investigation in both basic and applied research. Large scale production, cost effectiveness and stability of nanoscale systems are among key issues for their deployment in specific applications. In this regard, size and shape controlled nanosystems can be acquired through suitable fabrication techniques. Essentially, an appropriate growth mechanism is the key to yield quality nanomaterial products while introducing the desired phase, shape and also narrow size distribution. The present chapter focuses on different approaches adopted for synthesizing undoped and doped Gd_2O_3 nanoscale structures. The structural, optical and morphological evolutions are also highlighted.

Pure and doped Gd_2O_3 nanosystems have been fabricated via physicochemical and hydrothermal routes. The crystallographic information was revealed through a Rigaku miniFlex X-ray diffractometer (XRD) that employs a CuK_α source (λ=1.543 Å). The diffraction angle (2θ) was varied in the range of 20°–60°, and in steps of 0.05^o. Transmission electron microscopy (TEM) images were obtained either from a JEOL JEM 2100 or a TECNAI G2 20 S-TWIN machine, operating at an accelerating voltage of 200 kV. The selected area electron diffraction (SAED) pattern also performed with the help of TEM. The room temperature electron paramagnetic resonance (EPR) responses have been acquired on a JEOL: JESFA200 EPR spectrometer and considering a frequency 9.37 GHz and field modulation 100 kHz. The optical absorption spectra have been recorded on a UV-Visible spectrophotometer (Model UV2450, Shimadzu Corporation, Japan) working in the range of wavelength 200-700 nm. The room temperature PL spectra of the samples were revealed by using a LS 55 PerkinElmer spectrophotometer. The room temperature vibrational features were explored by a micro-Raman spectrometer (Renishaw, UK) and considering an excitation wavelength 514.5 nm of Ar^+ line. Moreover, for magnetic measurements were carried out on an SQUID (Evercool SQUID VSM DC magnetometer, Quantum design, USA).

2.2 Gd₂O₃ nanoparticles

2.2.1 Synthesis and characterization of undoped and Tb³⁺ doped Gd₂O₃ nanoparticles

First, gadolinium acetate hydrate [$Gd(CH_3CO_2)_3 \cdot H_2O$] (GdAc, CDH, 99.9% pure) is dispersed in deionized water and then a 1:1 molar sol has been prepared with citric acid [99% pure, CDH] under vigorous stirring for 30 min. The mixture is placed in an open-air oven at a temperature of 70°C in order to facilitate chemical reduction of GdAc to $Gd(OH)_3$ and to remove away the undesired water content. The product was further sintered in a tubular furnace and at a temperature of 400°C for 4 h. Later, the product is calcined at a temperature of 800°C for 2 h so as to discard byproducts and carbon-rich compounds. For synthesizing Tb³⁺ doped Gd₂O₃ product, terbium acetate Tb $(CH_3CO_2)_3 \cdot H_2O$] (TbAc, CDH, 99.9% pure) is added to the reaction mixture in the initial stage of the reaction, whereas rest of the reaction steps were kept similar as mentioned above. Quantitatively, in order to make 0.5, 1, 3 and 5% Tb³⁺ doped Gd₂O₃ powders, the Gd to Tb molar ratio was varied as 0.005, 0.01, 0.03 and 0.05; respectively. The flow chart of the overall procedure is illustrated in Figure 2.1.
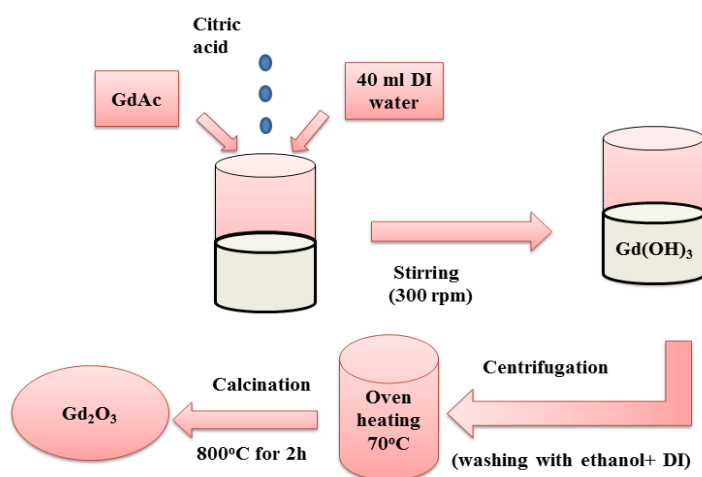

Figure 2.1: Synthesis protocol for preparing Tb³⁺ doped Gd₂O₃ nanosystems

Figure 2.2 (a) shows a series of the XRD patterns, of undoped and Tb^{3+} doped Gd$_2$O$_3$ nanoparticles. The four prominent peaks, located at 28.50, 33.10, 47.60, and 56.55^o corresponded to (222), (400), (440) and (622) crystallographic planes. With a preferred orientation along (222) plane, the patterns characterize cubic crystalline phase of Gd$_2$O$_3$ (JCPDS No.11-0604) [1]. As no appreciable peak shifting was noticeable in case of Tb-doped Gd$_2$O$_3$ system, the Tb^{3+} ions are expected to have undergone substitutional doping at Gd^{3+} sites [1].

The average crystallite size (d) and microstrain (η) can be calculated from the Williamson-Hall (W-H) expression (Appendix III) [2]:

$$\beta \cos \theta = 0.9\, \lambda / d + 4\, \eta \sin \theta, \qquad\qquad\qquad (2.1)$$

where β is the full width at half maxima, 2θ is the Bragg diffraction angle in degrees, λ is the wavelength of X-ray (1.543 Å). From W-H plots, the average crystallite size was found to be in the range of 11 - 24 nm and with the average size nearly doubled for the doped system as compared to its undoped counterpart (Table 2.1). The microstrains are of the order of 10^{-3} and 10^{-4}. While exhibiting a negative microstrain (10^{-3}), the undoped Gd$_2$O$_3$ nanopowder was believed to be comprised of much relaxed crystallites. With Tb doping, however, microstrain becomes positive (10^{-4}). Though the magnitude is ~10 times smaller than the undoped case, a reasonable lattice mismatch and consequently, internal stress might have occurred due to inclusion of Tb^{3+}. The magnitude of microstrain is doubled when the doping level reached ~5%.

The morphological feature of the nanoparticles is revealed through HRTEM imaging, depicted in Figure 2.2 (b). The size distribution of the nanoparticles systems is shown as figure-inset, in the form of a histogram plots. The average diameter of the nearly spherical nanoparticles is found to be approximately 30 nm.
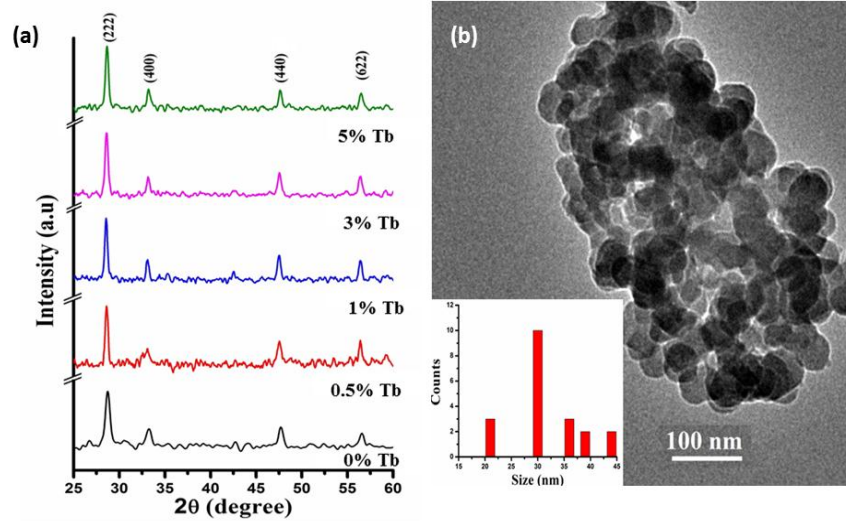
Figure 2.2: (a) A series of X-ray diffractograms of undoped and Tb³⁺ doped Gd₂O₃ nanophosphors, (b) HRTEM micrograph of the nanoscale Gd₂O₃ system.

Table 2. 1: Properties of Tb³⁺ doped Gd₂O₃ nanocrystalline phosphors

Tb concentration (%)	Avg. crystallite size (d) (nm)	Microstrain (ε)
0	11.8±2.1	-2.15×10^{-3}
0.5	21.6±2.3	2.35×10^{-4}
1.0	24.7±1.2	2.18×10^{-4}
3.0	24.7±1.5	1.98×10^{-4}
5.0	24.4±1.2	4.32×10^{-4}

2.2.2 Optical characteristics of undoped and Tb³⁺ doped Gd₂O₃ nanoscale systems

Optical absorption spectra of the un-doped and Tb³⁺ -doped Gd₂O₃ nanoparticles are shown in Figure 2.3. The samples show three characteristic peak maxima located at ~ 254 nm, 274 nm and 350 nm. Know that, the energy absorption in Gd is mediated via transition of 4f electrons to 5d level and then reorganization of the 4f electrons into various multiplets [3]. The seven electrons in the 4f orbitals of Gd have as many as 3432 multiplets and the ground state is $^{8}S_{7/2}$ [3]. Among these multiplets, the low lying multiplet above the ground state is $^{6}P_{7/2}$. The absorption peak at ~274 nm is typical for Gd₂O₃

particles and is attributed to $^8S_{7/2} \rightarrow {}^6I_{7/2}$ transition. Possibly, the weak peak at ~254 nm is due to one of the transition corresponding to $^8S_{7/2} \rightarrow {}^6I_{j/2}$ multiplets where j=9, 12, 13, 15 and 17 [4]. The peak at ~350 nm is ascribed to the $^6P_{7/2}$-$^8S_{7/2}$ of Gd(III) [5].

With the symbols having their usual meaning, and using generalized Tauc relation [6]: $(\alpha h\upsilon)^{1/n}=A(h\upsilon\text{-}E_g)$, one can estimate optical band gap of the systems under investigation. Here $h\upsilon$ is the incident photon energy, α is the absorption coefficient, E_g is the optical band gap, and A is the system dependent parameter. Assuming all transitions are direct, and allowed type (n=1/2), the estimated E_g values was found to decline with increase in Tb³⁺ doping. As for the undoped Gd₂O₃ phosphor, E_g= 5.22 eV and in consistency with an earlier report [7]. For 0.5, 1, 3 and 5% Tb doped systems, the gap was estimated as ~5.18, 5.17, 5.16 and 5.14; respectively. The reduction of the fundamental band gap with increasing doping concentration suggests creation of intermediate states below the bottom of the conduction band. The localized states could either be due to the presence of adequate oxygen vacancies or/and impurity states due to Tb-incorporation. Also, band gap follows a decreasing trend with the increase in size of the crystallites [8].
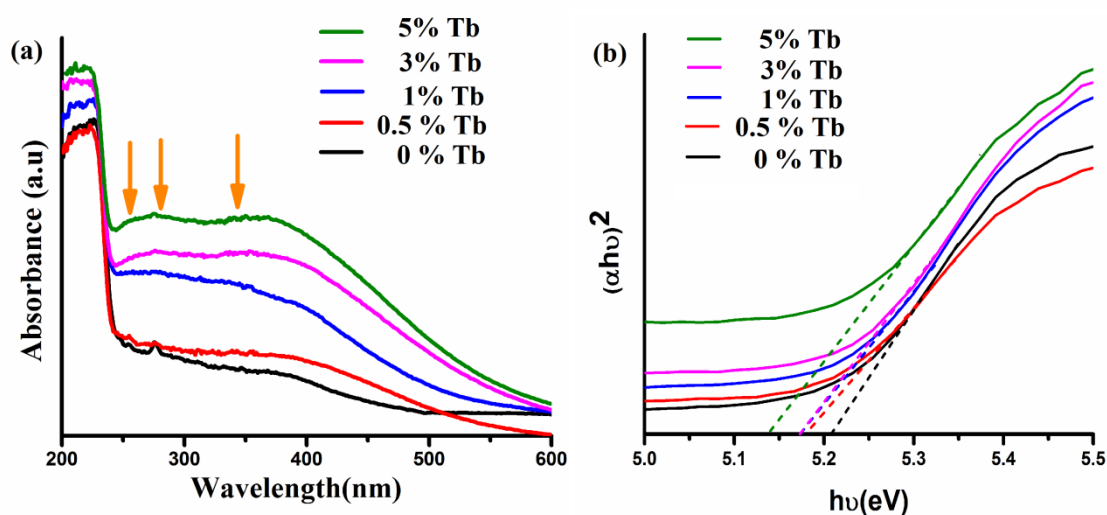

Figure 2.3: (a) Optical absorption spectra of undoped and Tb³⁺ doped Gd₂O₃ nanophosphors. Tauc plots of respective samples are shown in (b).

Furthermore, we have calculated the refractive indices (μ) of the nanophosphors using popular Dimitrov formula [9]:

$$\mu^2-1/\mu^2+2= 1-\sqrt{(E_g/20)} \qquad\qquad (2.2)$$

For the undoped Gd_2O_3 phosphor, $\mu= 1.97$ [10]. It has increased to 1.976, 1.977, 1.979, and 1.982 for 0.5, 1, 3 and 5%doped Gd_2O_3 systems. In other words, refractive index is improved by ~0.6% for a maximum Tb^{3+} doping (of 5%). Accordingly, the doped systems are optically more dense as compared to the undoped Gd_2O_3 counterpart. Thus the material becomes optically more active in view of inclusion of additional localized states into the system.

The PL emission spectra of the undoped and Tb^{3+} doped Gd_2O_3 nanophosphors (under 300 nm excitation) are depicted in Figure 2.4. In a typical spectrum, three main emission peaks were found to be located at ~432 nm, 450 nm and 492 nm but with variable emission intensities. The peak positions have been extracted through normalized multipeak Gaussian fitting such that the area under the experimental curve and the empirical curve remains same. The peak maxima at ~432 and 450 nm can be attributed to the surface defects of Schottky and Frankel kinds, whereas the peak maxima at ~492 nm are attributed to the self-trapped exciton luminescence [11]. Note that, in case of Tb^{3+} doped Gd_2O_3 system, the emission peak at ~492 nm is adequately improved owing to superimposition of $^5D_4 \rightarrow {}^7F_6$ related transitions of Tb^{3+}, which occur almost in the same wavelength regime. However, the transitional events are rather low for a higher level of Tb^{3+} doping. Interestingly, the broad emission peak at ~548 nm is most intense for the 0.5% Tb^{3+} doped Gd_2O_3 system as compared to other samples. The green emission due to the Tb^{3+} mediated $^5D_4 \rightarrow {}^7F_5$ transition, which is absent in case of the undoped system, was found to get quenched for a higher amount Tb^{3+} inclusion. There is a possibility that some interstitial sites can be occupied at higher doping levels of Tb^{3+}. We speculated that this transition is mediated by Tb^{3+} ions present in the interstitial sites. Since diffraction technique differs from spectroscopy technique this could not be ascertained.
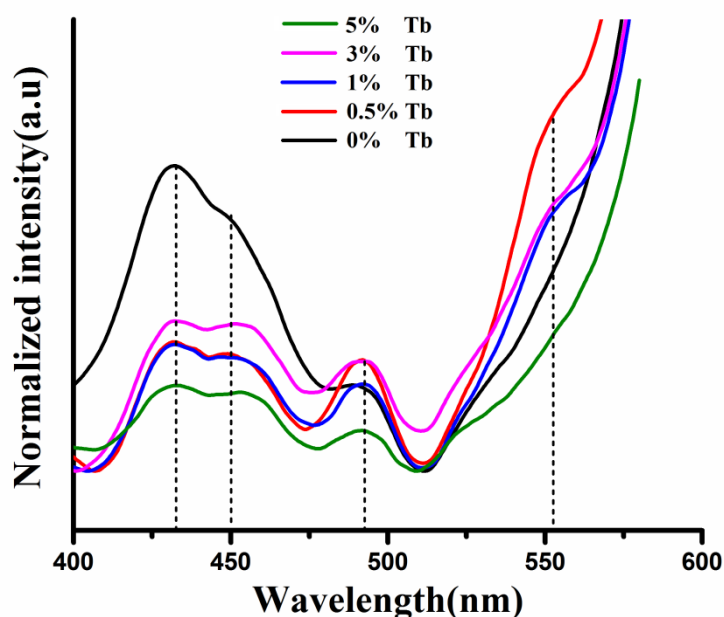
Figure 2.4: Room temperature photoluminescence spectra of the undoped and Tb^{3+} doped Gd$_2$O$_3$ nanophosphors (λ_{ex}= 300 nm).

The PL intensity ratio between $^5D_4 \rightarrow \ ^7F_5$ and $^5D_4 \rightarrow \ ^7F_6$ transitions was estimated to be 3.8 for 0.5% Tb doping case, whereas it is approximately 2.4 for 1% and 3% Tb-doping cases. Thus it is clear that, only an increment of Tb^{3+}-doping level cannot induce intense green emission responses. Although in a solvent media, Eu^{3+} or Tb^{3+} doped nanometric Gd$_2$O$_3$ gives a maximum emission signature corresponding to a dopant concentration of 5–6% [12], we predict that solid Gd$_2$O$_3$ powder could act as an efficient green phosphorescent candidate when the doping level is ~0.5%. This is because, the presence of hydroxyl groups, present on the nanocrystallites, can quench the emission response significantly. It is also worth mentioning here that, for a high doping level one may have to sacrifice some amount of crystallinity in the desired system.

The room temperature time resolved photoluminescence (TR-PL) data of 1% and 5% Tb^{3+} doped Gd$_2$O$_3$ nanosystem measured for emission wavelengths value λ_{em} =490, and λ_{em} =545 nm are shown in Figure 2.5. The decay curve followed a bi-exponential function, given by equation [12]
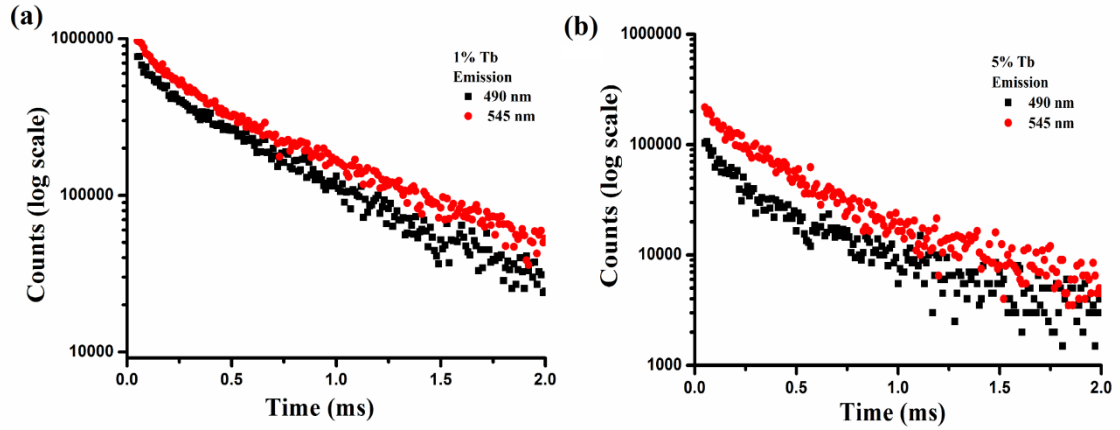
Figure 2.5: TR-PL spectra of (a) 1% and (b) 5% Tb doped Gd₂O₃ nanoparticles. Black and red experimental curves represent the nature of PL decays corresponding to λ_{em} = 490 nm and 545 nm, respectively.

$$A = A_1 e^{-t/\tau_1} + A_2 e^{-t/\tau_2} \qquad\qquad (2.3)$$

where τ_1 and τ_2 are the decay time constants associated with the fast and slow processes and A_1 and A_2 as corresponding emission intensities.

The time constants associated with the 490 nm and 545 nm emissions are shown in Table 2.2. The decay life time of our samples is much lower than the predicted ones in the earlier report [12]. This effect is may be due to the fast energy dissipation by the existence of numerous non-radiative recombination channels. Moreover, the presence of structural defects and hydroxyl groups could also lead to quenching in the emission profile thereby lowering the decay time [13].

Table 2.2 : Decay time constants calculated from TR-PL spectra

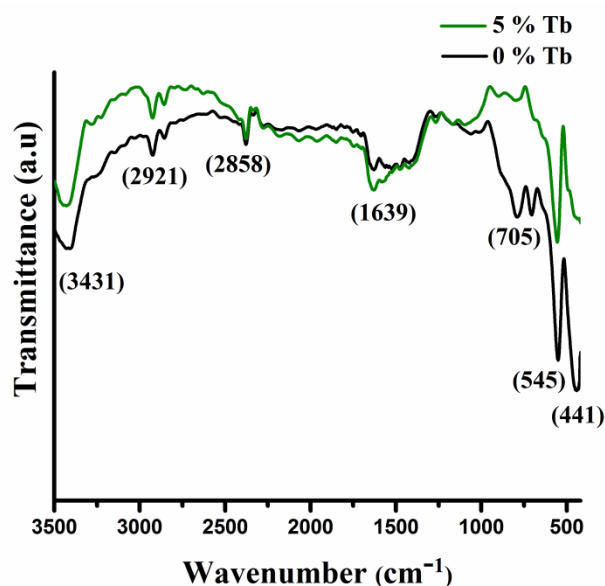| Sample	Emission wavelength (nm)	τ_1 (ms)	τ_2 (ms)
1% Tb	490	0.58	0.07
	545	0.11	0.64
5% Tb	490	0.49	0.93
	545	0.04	0.36

Figure 2.6: FTIR spectra of the undoped and Tb^{3+} doped Gd_2O_3 nanosystems.

Fourier transform infrared (FTIR) spectra of the undoped and 5% Tb^{3+} doped Gd_2O_3 phosphors are presented in Figure 2.6. The main bands located at ~ 2858 cm^{-1} and 2921 cm^{-1} can be assigned to the symmetric, asymmetric stretching vibrations of -CH_2 [1]. The band at ~705 cm^{-1} is the C-O vibration of the synthesized sample [14]. The bands at ~3431 cm^{-1} and 1639 cm^{-1} are attributed to the O-H stretching vibration and bending of water molecules. Whereas, the bands at located ~545 cm^{-1} and ~441 cm^{-1} are caused by the stretching vibration of Gd-O of cubic Gd_2O_3 [15]. It may be noted that, while other vibrational modes are not substantially modified, the strength of Gd-O vibrational stretching is adequately improved for the Tb^{3+} doped Gd_2O_3 nanosystem.

2.3 Gd₂O₃ nanorods

2.3.1 Synthesis and characterization of Gd₂O₃ nanorod powders

A simple hydrothermal procedure is carried out to grow quality Gd_2O_3 nanorods. In a typical procedure, 0.28 g of bulk Gd_2O_3 (Otto, 99.9%purity) is first dispersed in 40 ml distilled water followed by dropwise addition of dil. HNO_3 until a clear sol is obtained. The pH of the mixture is then adjusted to 9.2, 10.8, and 13.3 by adding several drops of 5M NaOH solution under vigorous stirring (~300 rpm). The mixture is then transferred to a teflon-lined stainless

steel autoclave and subjected to oven heating at a temperature of ~140°C, for 24 h. A white solid product of $Gd(OH)_3$ is now collected by filtering the precursor using a whatman filter®. In the next step, the product was washed several times, first with distilled water and then with ethanol, followed by oven-drying at a temperature of 80°C. Finally, the hydroxide powder is annealed at 600°C, for 3h. The spontaneous decomposition and subsequent dehydration of $Gd(OH)_3$ is believed to be facilitated, yielding Gd_2O_3 nanorod product. The chemical reaction steps and flow chart diagram of hydrothermally synthesized Gd_2O_3 nanorods are as described below .
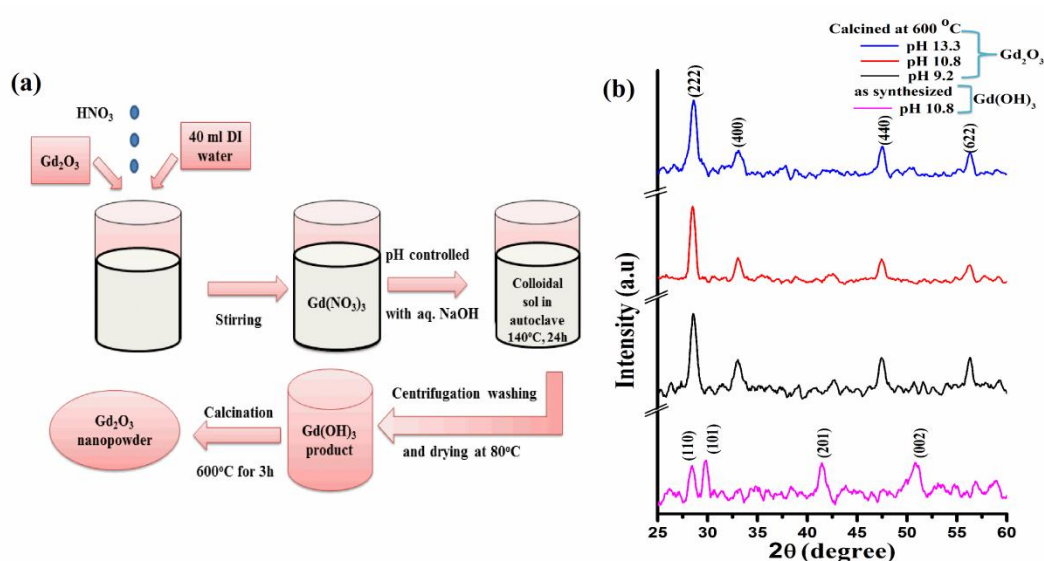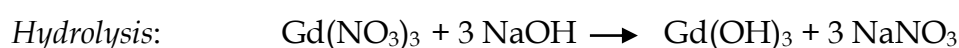
Acidification: $Gd_2O_3 \text{ (bulk)} + HNO_3 \longrightarrow Gd(NO_3)_3 + 3\,H_2O$

Hydrolysis: $Gd(NO_3)_3 + 3\,NaOH \longrightarrow Gd(OH)_3 + 3\,NaNO_3$

Dehydration: $2\,Gd(OH)_3 \longrightarrow Gd_2O_3 \text{ (nanopowder)} + 3\,H_2O$
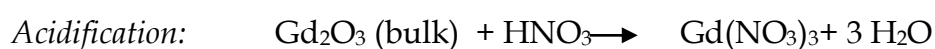
Figure 2.7: (a) Block diagram of hydrothermally synthesized Gd₂O₃ nanorods, (b) XRD patterns of as-synthesized Gd(OH)₃ product (pH 10·8) and Gd₂O₃ nanorods derived from precursors of different pH control.

The XRD patterns of as-synthesized $Gd(OH)_3$ product prepared at pH = 10·8 and Gd_2O_3 nanorod-powders prepared at pH = 9·2, 10·8 and 13·3 are depicted in Figure 2.7(b). The hydroxide product exhibited a hexagonal crystal structure with observable diffraction peaks indexed as (1 1 1), (1 0 1), (2 0 1) and (0 0 2) crystallographics planes (JCPDS no. 83-2037) [16]. After sintering at a

temperature 600°C, prominent, yet apparently broadened diffraction peaks corresponding to (2 2 2), (4 0 0), (4 4 0) and (6 2 2) crystallographic planes are obtained ensuring the existence of a cubic crystalline phase (JCPDS no. 11-0604) [1]. No peak due either to hydroxides, impurities or byproducts has been detected.

With symbols having their usual meanings and using diffraction formula relevant to cubic phase:

$$d_{hkl} = (h^2+k^2+l^2/a^2)^{1/2} = \lambda/2\ sin\theta \qquad\qquad (2.4)$$

The lattice parameter ($a=b=c$) of the samples synthesized at pH of 9·2, 10·8 and 13·3, are estimated to be 10·80, 10·83 and 10·79 Å, respectively. Earlier, a cubic-phase cell parameter of magnitude 10·81 Å has been predicted for the Gd₂O₃ system [17]. The average crystallite size (d) and microstrain (η) can be calculated by using popular W–H expression as mentioned in equation (2.1). The average crystallite sizes are found to be ~ 5·19, 6·46 and 6·09 nm as for pH 9·2, 10·8 and 13·3 cases, respectively (Table 2.3).

Table 2. 3. Average crystallite size (nm), lattice parameter (nm), microstrain and dimension of nanorods (nm) of as-synthesized Gd₂O₃ nanorod systems.

Nanorods synthesized from precursors	Avg. crystallite size (d) (nm)	Lattice parameter ($a=b=c$) (nm)	Microstrain (x10⁻³)	Dimesion of nanorods		
				Length (nm)	Diameter (nm)	Aspect ratio
*pH 9.2	5.19	1.080	-12.7	---	---	---
pH 10.8	6.46	1.083	-8.9	75-115	19	~4
pH 13.3	6.09	1.079	-8.5	60-128	7	~8.5

*TEM analysis not performed on this sample.

The HRTEM images of the nanorod samples, prepared at pH 10.8 and pH 13.3, are shown in Figure 2.8 (a) and (b). As for pH 10.8 specimen, a number of nanorods with an average diameter ~19 nm and length ranging from 76 to 115 nm can be evident in the micrograph (Figure 2.8(a)). With a smoothened surface, the rods resemble the structure of 'unfold fingers'. Note that, for any nanorod, the diameter at the middle of the rod is much larger than at the edge. This is ascribed to the spontaneous decomposition of gadolinium hydroxide

into its oxide product followed by subsequent assimilation of crystallites along (222) plane and instant termination at the end. Also, all the Gd$_2$O$_3$ nanorods were not found in the same focal plane and that is why we observed a reasonable difference in the image contrast of many off-aligned rods. As for sample synthesized from a precursor of pH 13.3, the range of average nanorod length was found to be wider i.e., 60-128 nm but having a lower average diameter ~ 7.1 nm (Figure 2.8 (b)). Thus, both shorter and longer rods could be achievable at a higher pH. We believe that, unrestricted preferential growth of nanocrystallites might have led to longer sized rods. But shorter nanorods could have been developed due to obstruction of one nanorod growing in the vicinity of the other or, thermodynamic instability that would keep surface energy of the overall system minimum. Consequently, the diameter of the rods can also be reduced in this case. As diameter is close to the average crystallite dimension (see, XRD analysis) we expect that, aligned growth is manifested by just piling up of single crystallites along the preferential direction. Whereas, nanorods derived from a precursor of lower pH (=10.8), comprise of several crystallites along a direction normal to the preferential growth, thereby resulting in a larger diameter (~19 nm) of the rods. Considering the lower limit of the nanorod length, the aspect ratio was estimated to be ~4 and 8.5 corresponding to pH=10.8 and 13.3 cases; respectively (Table 2.3). A higher pH value represents a higher concentration of OH$^-$ ions and a higher chemical potential of the precursor solution. A higher chemical potential is generally preferable for the growth of higher aspect ratio 1D nanostructures [18]. Here, a nanorod with a higher aspect ratio is obtainable at a higher pH, but along with some amount of inhomogeneity. Figure 2.8(c) shows an enlarged view of a particular region of the nanorod. The clear lattice fringe pattern suggests crystalline nature of the nanorod, giving an interplanar spacing of ~0.312 nm and corresponding to the (222) crystallographic plane of the nanosystem. This is in accordance with the XRD pattern of the concerned specimen (pH=10.8). The SAED pattern exhibits a number of arrayed bright spots indicating highly crystalline nature of the specimen under study.
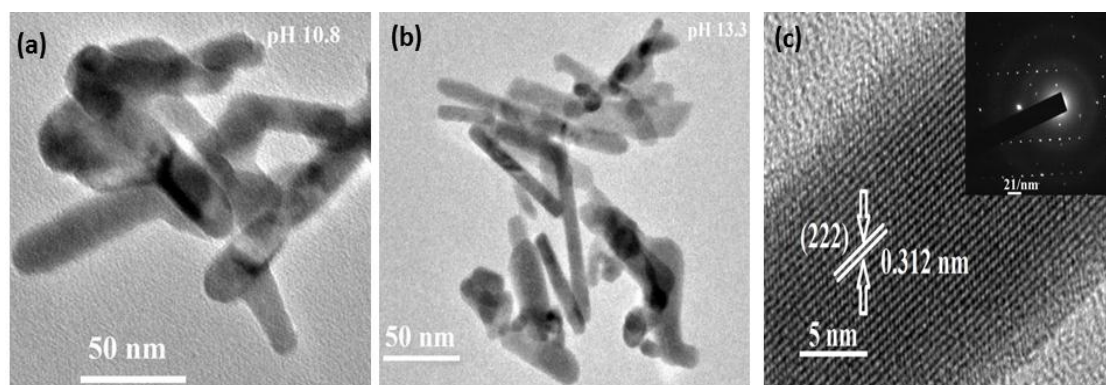
Fig.2.8: (a) and (b) represent HRTEM images of the Gd_2O_3 nanorods samples synthesized at pH 10.8 and 13.3, respectively. Magnified image of an isolated Gd_2O_3 nanorod (derived from pH 10.8 precursor) with crystal lattice fringes is depicted in (c). The SAED pattern is being highlighted in the inset of (c).

The growth mechanism of Gd_2O_3 nanorods has been illustrated schematically, in Figure 2.9. The growth of Gd_2O_3 nanorods is believed to be governed by a solution-solid phase process [19]. In the hydrothermal process, several drops of aq. NaOH are normally added to adjust the pH of the sol. According to Xu et.al, the growth is neither governed by a catalyst nor directed by any template [20]. On adding aq. NaOH, the Gd^{3+} ions of the nitrate product tend to interact with the OH^- ions in the solution phase. On adding NaOH, a gentle white solution is created which comprised of colloid particles. The colloids, while partially dissolved in water results in a metastable supersaturated solution under hydrothermal environment. On cooling back to room temperature, a large number of seed particles are formed through homogenous nucleation process. It is the seed which becomes the basis of 1D elongated nanostructures formed as a result of coherent re-crystallization process. Accordingly, the whole supersaturated solution is recrystallized to yield highly crystalline rod-shaped structures [20].

With an electronic configuration of [Xe] $4f^7$, Gd^{3+} has half-filled shells having a $^8S_{7/2}$ ground state [3]. As we know, the energy absorption in Gd is mediated via transition of $4f$ electrons to $5d$ level and then reorganization of the $4f$ electrons
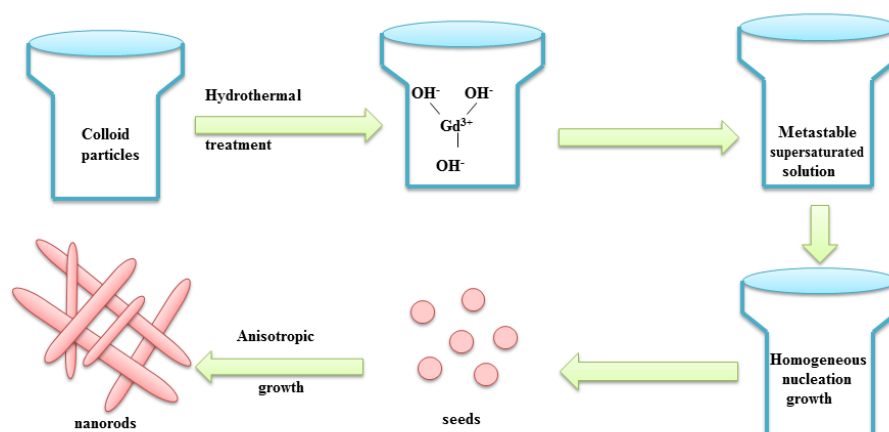
Figure 2.9: A scheme of growth mechanism illustrating formation of Gd$_2$O$_3$ nanorods.

into various multiplets. The low lying multiplet above the ground state is $^6P_{7/2}$. Essentially, two absorption peaks have been observed in the spectra shown in Figure 2.10. The absorption peak positioned at ~ 274 nm is typical for Gd$_2$O$_3$ nanorods and can be attributed to $^8S_{7/2} \rightarrow {}^6I_{7/2}$ transitions [3]. The peak positioned at ~ 400 nm, can be assigned to recombination of delocalized electrons close to the conduction band with a single charged state of surface oxygen vacancy as per Wang's proposition [21]. The peak at ~ 274 nm has a strong absorption feature, particularly for the nanorod specimen derived at a higher pH value.
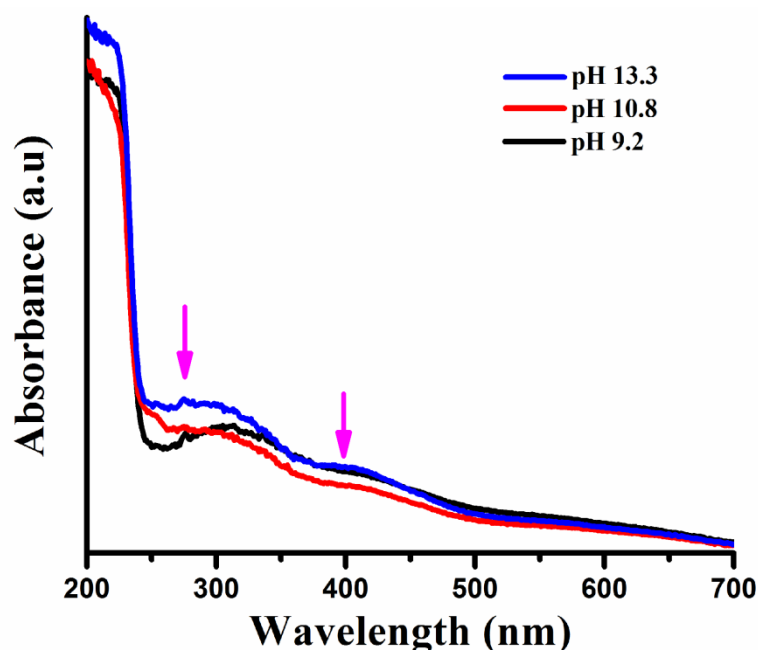

Figure 2.10: Absorption spectra of Gd$_2$O$_3$ nanorods synthesized at different pH.

Photoluminescence spectroscopy is a powerful technique to understand the nature of radiative transitions and defect related emission response of a material system. The room temperature emission spectra of the Gd$_2$O$_3$ nanorods, excited at a wavelength of ~ 300 nm are shown in Figures 2.11(a–c). The PL spectra represent characteristic radiative emission features of the nanorods synthesized at different pH values. The asymmetrically broadened spectra signify the superimposition of several peaks of different origin. The deconvolution of each of the spectra through multiple Gaussian fitting could help extracting independent peaks, which can be found in Figures 2.11(a–c). All the samples have showed three prominent peaks, at ~ 413, 442 and 472 nm. The band to band emission was not observable due to the improved defect related emission response. The peak maxima at ~ 413, 442 and 472 nm could be attributed to the surface defects of different Schottky and Frenkel types [11]. The normalized intensity ratio of ~ 413 to 472 nm peak increases with increasing pH value of the desired precursor. In oxide systems, typically oxygen vacancies and interstitials are vastly prevalent and the manifestation of such defects, contribute significantly to the modified luminescence phenomena. Figure 2.11(d) shows a photoluminescence excitation (PLE) spectrum of Gd$_2$O$_3$ nanorods (pH=10·8) monitored at an emission wavelength of ~ 480 nm. PL excitation spectroscopy is a useful method to investigate the electronic structure of the materials with low absorption features. The wavelength of the excitation light is monitored, for a fixed emission wavelength of the material being studied. The peaks, in the PLE spectrum, often represents absorption characteristics of the system under study. Basically, Gd^{3+} has a simpler absorption spectrum in comparison to the other trivalent RE ions. Note that, the ground state energy level for Gd^{3+} is $^8S_{7/2}$ level. As can be found, the excitation spectra has clearly revealed four important peaks, positioned at ~ 230, 248, 260 and 282 nm. The 230 nm emission peak is attributed to the excitation band of Gd$_2$O$_3$ host [22]. The peak at ~248 nm is ascribed to one of the transitions corresponding to $^8S_{7/2} \rightarrow {}^6I_{j/2}$ multiplets, where j=9, 12, 13, 15 and 17 [4]. The

band observed at ~260 nm is assigned to $^8S_{7/2} \rightarrow {}^6D_{9/2}$ transition [23], whereas the peak at ~282 nm corresponded to the $^8S_{7/2} \rightarrow {}^6I_{7/2}$ transition [4].
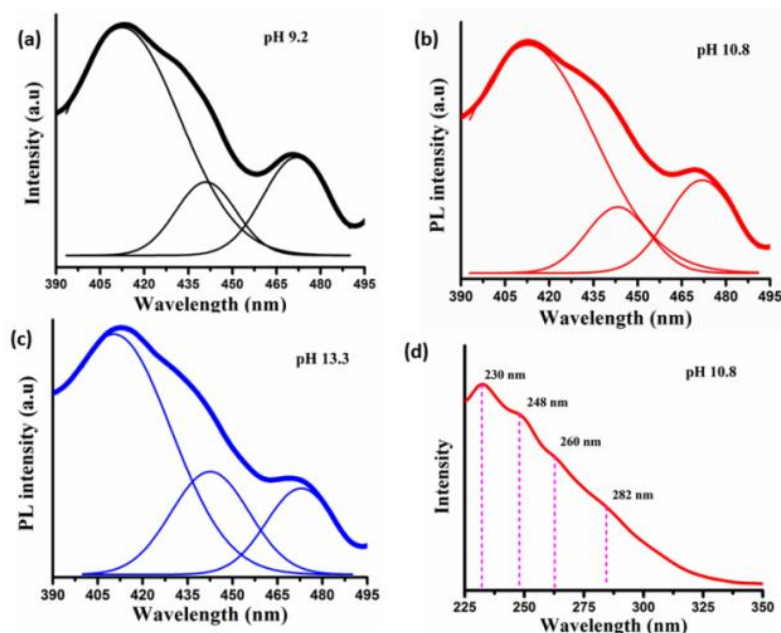

Figure 2.11: Room temperature PL emission spectra λ_{ex}= 300 nm with deconvolution of Gd₂O₃ nanorods obtained from precursors at (a) pH 9·2, (b) pH 10·8 and (c) pH 13·3. a) PL excitation spectrum (λ_{em}= 480 nm) for pH=10.8 sample is shown in (d).

Thermogravimetric analysis (TGA) was employed to evaluate the weight loss during progressive heating. Figure 2.12 shows the nature of weight loss in the range of 27-600°C at an atmospheric pressure. In the range 27-250°C, the weight loss (2.11%) is essentially due to the dehydration of absorbed H_2O in Gd(OH)₃ system. In the range, 250°C-350°C the weight loss is approximately 8.01%, whereas 350°C to 426°C with weight loss 1.3%. The decomposition of Gd(OH)₃ to GdOOH is expected between 250°C -426°C. In final step at 426-594°C with weight loss 2.2% is due to GdOOH to Gd₂O₃. The total weight loss measured 13.62%, which almost comparable to the theoretical calculation of Gd(OH)₃ (13.03%) calculated from the reaction of their complete decomposition to produced Gd₂O₃ [20].
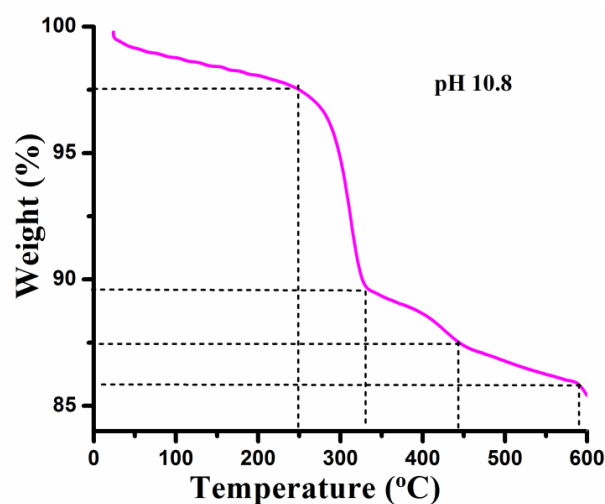
Figure. 2.12: Thermogravimetric analysis of unsintered Gd(OH)₃ product (pH= 10·8).

Raman spectroscopy is a versatile but non-destructive tool to explore vibrational, rotational and other low frequency modes in the systems under study. Raman spectra of the Gd_2O_3 nanosystems are depicted in Figure 2.13(a). Both the Gd_2O_3 nanoparticles (GNP) and Gd_2O_3 nanorods (GNR) exhibited a prominent peak, positioned at ~360 cm^{-1} and is attributed to the collective signature of F_g and E_g modes as predicted in case of the cubic phase Gd_2O_3 system [24]. While the peak position is retained, the Raman intensity of the GNR system is seen to be improved as compared to the GNP system. Upon Lorenzian fitting of the Raman peak (F_g+E_g mode), the FWHM corresponding to GNP and GNR systems, are calculated to be ~25.9 and 17.5 cm^{-1}; respectively. The decrease of FWHM of GNR system indicates an enhanced crystallinity along with a stronger phononic response [25]. The phonon life time (τ) of the synthesized samples can also be obtained from the Raman spectra through the energy time uncertainty relation [25]:

$$\frac{1}{\tau}=\frac{\Delta E}{\hbar}=2\pi c\Gamma, \tag{2.5}$$

where ΔE is the uncertainty in the energy of the phonon mode, $\hbar$ is the reduced Planck's constant and Γ is the FWHM of the Raman peak in unit of cm^{-1}. The phonon lifetimes of our GNP and GNR systems are calculated to be 0.20 and 0.32 ps; respectively. Thus, the one-dimensional nanorods (GNRs) are capable

of preserving phononic modes for a longer duration than the modes available in the nanoparticle (GNPs) counterpart.

In order to assess magnetic behaviour of the synthesized product, the Gd_2O_3 nanorod sample (prepared at a pH of 10.8) was assessed by a Quantum Design MPMS device. Superconducting quantum interference device (SQUID) is a very sensitive magnetometer used to monitor very small changes in magnetic flux and to reveal the magnetic polarization in response to an applied field. The working principle of a SQUID is based on the superconducting loops containing Josephson junctions. The details can be found in literature (Appendix IV) [26]. Figure 8 (b) shows the SQUID magnetometry magnetization vs. magnetic field (*M-H*) plot measured at room temperature (300 K). The magnetization response was measured when applied field was varied in the range -6 T to 6 T. A small hysteresis could be realized initially only upon zooming the central part of the plot. Thus the sample has a dominant paramagnetic phase at room temperature. Even the exact saturation magnetization (M_s) could not be predicted. The paramagnetic nature of the nanorods containing Gd^{3+} centers is due to the presence of half -filled *f* orbitals with seven electrons [4]. Note that, paramagnetic characteristic of a system is caused by a number of magnetic dipole moments summing up to zero in the absence of an applied field. But the net moment becomes nonzero when the system is subjected to a field. However, superparamagnetism arises when thermal energy is strong enough to orient individual moments randomly. As far as superparamagnetism is concerned, in the past, most of the studies were devoted mostly to iron based nanostructures [27]. We anticipate that, the paramagnetism in the Gd_2O_3 nanorods has arisen from the noninteracting localized nature of the magnetic moments. The magnetic properties of the Gd^{3+} ions come from seven unpaired inner 4*f* electrons, which are closely bound to the nucleus and effectively shielded by the outer closed shell electrons $5s^25p^6$ from crystal field. Among various paramagnetic RE ions, Gd^{3+} ions possess a high magnetic moment due to isotropic electronic ground state $^8S_{7/2}$. In order to explore further, we zoomed in the *M~H* response near zero field. Remarkably,

the M exhibits nonzero value in the absence of the field (H=0). The coercive field (H_c) and remanence (M_r) were found to be 0.0066 T and 0.0136 emu/gm; respectively. A low coercive field indicates that, magnetic moments can be reversed even by changing the direction of a weak field.
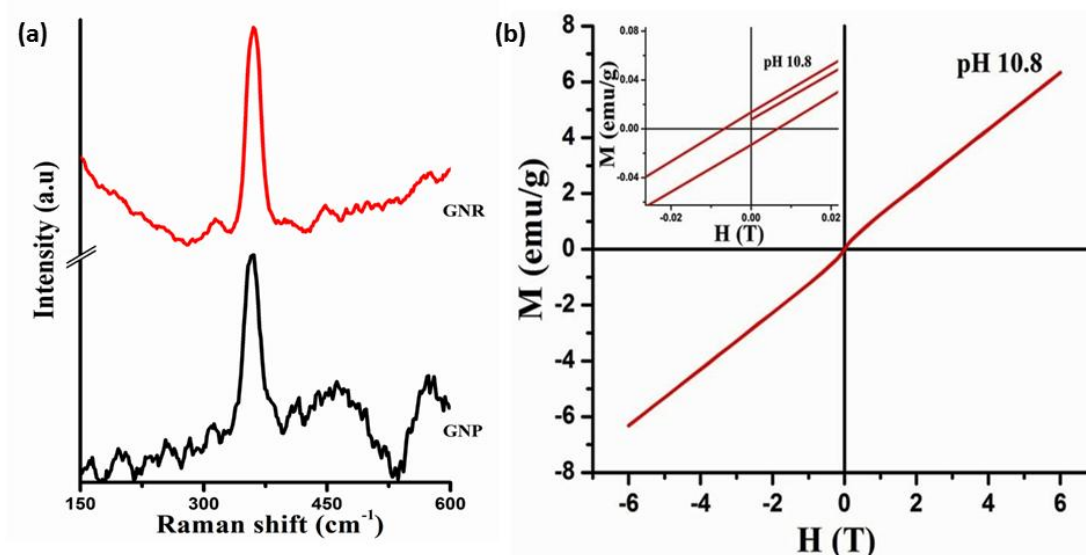

Figure 2.13:(a) Raman spectra of Gd₂O₃ nanoparticles (GNP) and nanorods (GNR), (b) room temperature $M \sim H$ plot of the Gd₂O₃ nanorods synthesized at pH=10·8. The inset shows enlarged view of the plot near zero-field.

2.3.2 Synthesis, growth mechanism of Gd₂O₃ nanorods obtained from nanoparticle seeds

At first, gadolinium acetate hydrate [Gd(CH₃CO₂)₃.H₂O] (CDH, 99.9% pure) is dispersed in deionized water and then, citric acid [C₆H₈O₇] (CDH 99% pure) is gently added to offer a 1:1 molar solution. The mixture is then subjected to vigorous stirring (~300 rpm) for 30 min, followed by filtration with a whatman paper® to yield Gd(OH)₃ product. The Gd(OH)₃ product is then further sintered at a temperature of 800 °C in a tubular furnace, for 4 h, which gave rise to yield Gd₂O₃ nanoparticles (GNP). The details procedure has been discussed in page no. 37.

Secondly, 0.15 g of the synthesized GNP is dispersed in 35 ml distilled water. The pH is adjusted to ~10 by adding aq. NaOH in a drop wise manner. The mixture is then transferred to a teflon-lined stainless autoclave and
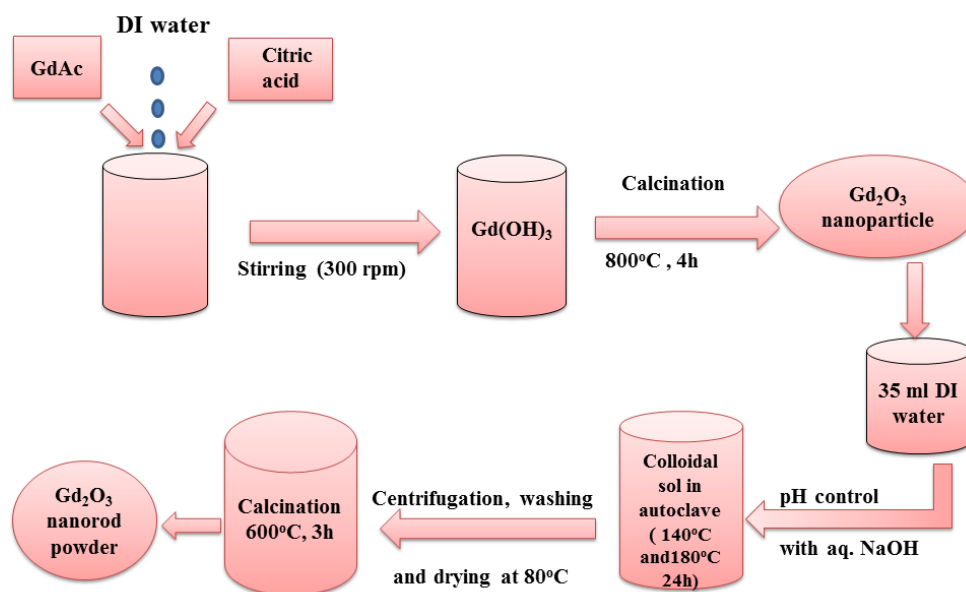
Figure 2.14: Block diagram on various steps involved in the synthesis Gd_2O_3 nanorods

subjected to oven-heating independently while maintaining a temperature of 140 ^oC and 180 ^oC, for 24 h. A white solid precipitate of Gd_2O_3 is then collected by filtering the precursor by using a Whatman filter®. The as-received product was washed several times, first with distilled water and then with ethanol, and subsequently followed by oven-drying at a temperature of 80 ^oC. In order to remove away all the hydroxyl groups present in the system, the powder was finally calcined at a temperature of 600 ^oC for 3 h. The as- received hydroxyl-free Gd_2O_3 nanorods (GNR) are kept ready for subsequent experimentation. The block diagram of the complete synthesis procedure is shown in Figure 2.14. Figure 2.15 (a) shows a set of XRD patterns of the as-synthesized samples of the Gd_2O_3 nanoparticles and hydrothermally processed Gd_2O_3 nanorods at different temperatures. In each case, the diffraction peaks characterize cubic phase of the Gd_2O_3 system [1]. The distinct peaks corresponded to (222), (400), (440) and (622) crystallographic planes of the samples under investigation ((JCPDS no. 11-0604) [1]. Moreover, we notice a shifting of peaks towards a lower diffraction angle (2θ) in case of Gd_2O_3 nanorods as compared to particles. The shifting of peak position towards a lower diffraction angle would indicate enhancement of lattice parameters [17]. Since (222) appeared as the most

intense peak, most of the crystallites are believed to have preferred orientation along the said plane. Moreover, the average crystallite size (d) and microstrain (η) can be calculated from the W-H expression mentioned in equation (2.1). The GNP system gives an average size (d) estimation of ~11.8 nm. Whereas, hydrothermally derived GNRs that are processed at a temperature of 140 and 180 °C, and post-calcined at a temperature of 600 °C offered an average crystallite size of ~12 and 14 nm; respectively. It may be noted that, without calcination, the GNRs experienced a relatively lower size of ~8 nm (Figure 2.15 (a) and Table 2.4). Using the diffraction equation valid for a cubic system (equation no. 2.4) the lattice parameter, 'a' is estimated to be 1.077, 1.086, 1.091 and 1.086 nm for GNP, GNR without calcination and GNRs (prepared at 140 and 180 °C) subjected to calcination at a higher temperature (Table 2.4). It may be noted that, particle-size dependent lattice expansion is quite common in numerous metal oxides including ABO_3 and ABO_4 types [28, 29]. According to these works, the lattice expansion is due to a proportionately large content of surface defect dipoles which could improve the negative surface stress with the particle size reduction. On the contrary, in our hydrothermally processed Gd₂O₃ nanosystems, we observed an increased lattice parameter with increasing crystallite size. Our results are consistent to those of a recent article by Yang and co-workers on $GdVO_4:Eu^{3+}$ system [30]. It was proposed that, calcination driven reduced negative surface stress could lead to the desired change [30].

Figure 2.15(b), (c) and (d) depict the HRTEM images of Gd₂O₃ nanoparticles and nanorods synthesized at a temperature of 140 and 180 °C; respectively. The average size of the nanoparticles, as found from the micrograph, is ~30 nm (Figure 2.15(b)). The sample processed at a temperature of 140 °C contained only a few fully grown nanorods along with many underdeveloped rods (Figure 2.15(c)). While exhibiting an approximate diameter of 32 nm, the nanorods as large as 170 nm could be realized. However, as can be evident from Figure 2.15(d), the GNR sample prepared at a temperature of 180 ° C, contained a number of fully grown nanorods with occasional hollow

appearances. The average length of the nanorods was found to vary in the range of ~155–190 nm and diameter ~33 nm (Figure 2.15(d)). The inset of Figure 2.15(d) basically depicts a SAED pattern that highlights equi-spaced bright spots arranged in a cubic lattice. Thus we, anticipate mono-crystalline nature of the GNRs synthesized at a temperature of 180 °C.
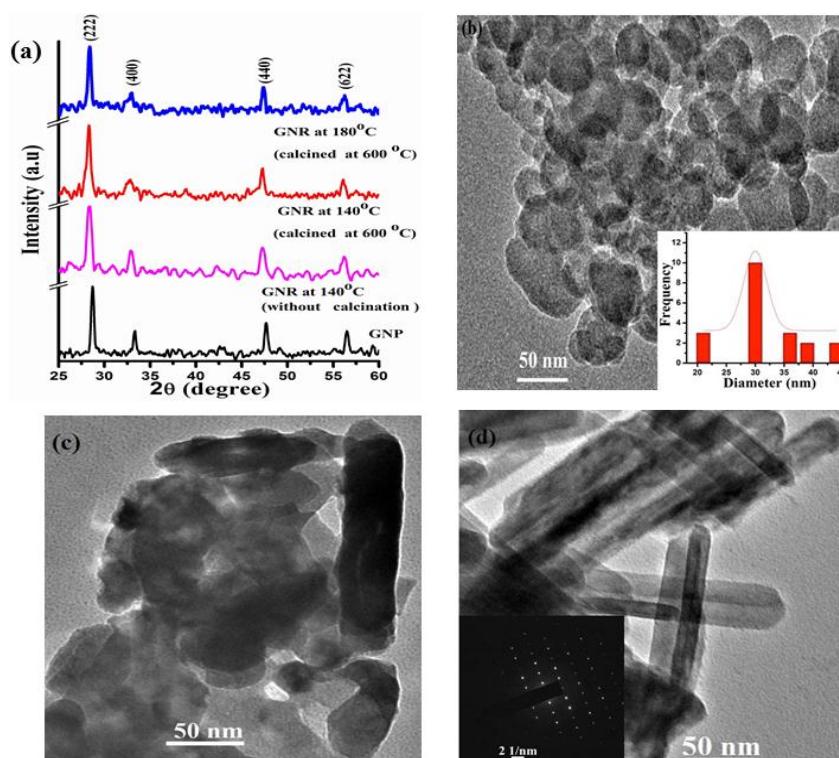

Figure 2.15: (a) XRD patterns of all the Gd₂O₃ nanosystems. HRTEM images of Gd₂O₃ (b) seed nanoparticles, and nanorods synthesized at a processing temperature of (c) 140°C, and (d) 180°C. The micrograph shown in (d), characterize well developed nanorods with instances of hollow morphology. The SAED pattern is depicted in the inset of (d).

Table 2.4: Physical characteristics estimated from XRD data

Sample	Average crystallite size (d) (nm)	Micro-strain (η) ($\times 10^{-3}$)	Lattice parameter ($a=b=c$) (nm)
GNP	11.8±1.1	-2.2	1.077
GNR 140°C	8±1.2	-5.4	1.086
GNR 140°C (calcined at 600°C)	12±1.4	-3.8	1.091
GNR 180°C (calcined at 600°C)	14±1.6	-1.7	1.086

The presence of fully evolved nanorods at an elevated hydrothermal temperature is attributed to the oriented attachment mechanism [31]. The formation of 1D nanostructure with a higher aspect ratio is essentially possible in presence of higher concentration of OH$^-$ ions [18]. The reaction temperature is another factor which could affect the aspect ratio of the Gd$_2$O$_3$ nanoscale structures. It is worth mentioning here that, either NaOH or KOH plays an important role in the growth of 1D nanorods. The pH dependent study of Gd$_2$O$_3$ can also be found in the literature [32]. A number of patterns, such as nanospheres, nanorods, nanowires, etc., have been grown through hydrothermal route and with necessary pH control [32,33]. Plate-type morphology are obtained for pH<7, whereas nanorods and nanowires are invariably developed at high pH values. Recently, we have also succeeded in fabricating Gd$_2$O$_3$ nanorods via a catalyst-free hydrothermal approach [34]. The effect of pH has been discussed along with the growth mechanism of the nanorods and apparently, nanorods with high aspect ratios can be revealed in the environment of high pH media. The addition of NaOH and KOH has also been found to help control the phase and morphology of octahedral Fe$_3$O$_4$ crystals as well as α-Fe$_2$O$_3$ platelets [35, 36].

The growth mechanism of Gd$_2$O$_3$ nanorods is schematically shown in Figure 2.16(a). The corresponding TEM imaging can be found in the lower panel of the same figure. Since the Gd$_2$O$_3$ nanorods are synthesized from the Gd$_2$O$_3$ nanoparticles, we speculate that particle growth would occur along a themodynamically favourable direction. Previously, melting assisted particle growth was observed due to swift ion impact as well as prolonged sintering [37, 38]. In either case, particle growth has been believed to be accompanied by Ostwald ripening (OR) mechanism. In general, particles obtained by OR mechanism have regular shape and the surface defects produced during growth vanish with the particle dissolution. However, since the model is purely based on the equilibrium condition between the solubilization and precipitation, and less amount of solubility is involved at the nanoscale level, an alternative strategy has been adopted. At nanoscale level, the growth

mechanism, under special circumstance, can be governed by oriented attachment (OA) mechanism [39]. Typically, OA mechanism is based on three factors: (1) dipole-dipole interaction that causes two oriented particles to get attached, (2) interaction prevails until perfect lattice match is ensured, and (3) the adjoining interface eventually vanishes resulting in a single crystal particle [40]. In other words, the nanorod structures can be produced by energetically favourable alignment and coalescence of neighboring particles through elimination of the common boundary. This is clearly evident from the micrographs placed in the middle of the lower panel, shown in Figure 2.16(a). The adjoining particles are indicated by dashed- yellow regions, and the interfaces, indicated by arrow marks in the magnified image.

Since the surface energy plays an important role in the crystal growth process, the growth of elongated nanostructures can occur by lowering the surface energy along a specific direction. The driving force behind anisotropic growth of nanostructures is the crystal surface reactivity [41]. In general, Gd$_2$O$_3$ is a known REO system and possesses a cubic crystal structure. Moreover, it is difficult to grow anisotropic nanostructures through classical OR mechanism. Previously, the OA mechanism was employed to describe the growth process in different oxide systems, such as, TiO$_2$ [42], CdTe [43], and Y$_2$O$_3$ [41]. In the present situation, at first, the cubic Gd$_2$O$_3$ nanoparticles aggregate due to dipole-dipole interactions, fused gradually and then, recrystallize into single crystalline nanorods. It may be noted that, in our case growth of the nanorods is neither surfactant assisted nor template based but purely governed by dipole-dipole interaction caused by OA.

Under hydrothermal treatment, nanoparticles are randomly oriented following Brownian motion. When two adjacent primary particles collide, the coalescence occurs and that, the particles share a common crystallographic orientation. Thus the two primary particles attach to each other and combine into a secondary one which is still very small and continue to collide and coalesce. The repetition of such an organized event leads to directed assimilation of
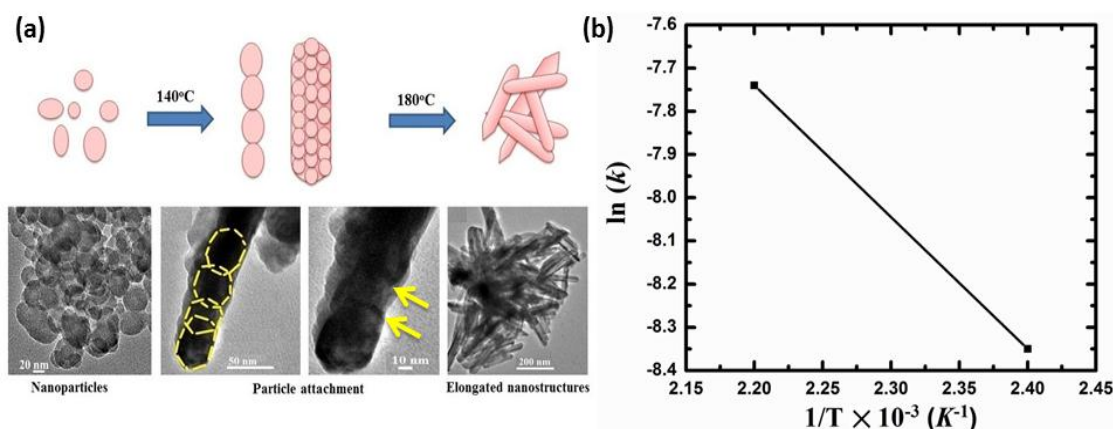
Figure 2.16: (a) Schematic growth mechanism of Gd$_2$O$_3$ nanorods (upper panel) and a set of TEM images illustrating transformation of nanoparticle seeds to nanorods through oriented attachment (lower panel), (b) Arrhenius plot of the reaction constant k vs. inverse of temperature, T^{-1}.

particles, resulting in rod shaped structures. The kinetic model governed by OA mechanism can be described by the following reaction [44]:

$$A_1 + A_1 \overset{k}{\rightarrow} B \quad , \tag{2.6}$$

where A_1 is a primary nanoparticle, B is the product of the coalescence of two primary nanoparticles and k is the rate constant involved in the reaction between the two particles. Essentially, reaction occurs between the primary nanoparticles (monomer), whereas nanorods are the collective outcome of the repetitive events. The kinetic model for the OA mechanism can be formulated by [44],

$$d_t = \frac{d_0\left(\sqrt[3]{2kt+1}\right)}{kt+1} \quad . \tag{2.7}$$

Here, d_o is the diameter of the precursor nanoparticles, d_t the diameter of the as grown nanocrystals at time t and k is the reaction constant. The values of k can be calculated for both the reaction temperatures, 140 and 180 °C. In the first case, substituting d_t=32 nm, d_o=30 nm and t=1440 min, in Eq. (2.7), k is calculated to be 2.36×10^{-4} min^{-1}. Using similar kinetics, the rate constant is found to be 4.34×10^{-4} min^{-1} for GNRs synthesized at an elevated temperature of 180 °C (diameter, d_t ≈33 nm). Note that, for evaluating k, we have not considered the whole length of the nanorods but diameter of the nanorods as

predicted from the TEM analyses. This is because, fully grown elongated structures coexist with the under-developed structures that would represent different stages of growth. The formation of nanorods is believed to be as a result of directed-multi step OA processes dictated by Eq. (2.7). In order to explore the relationship between the kinetic constant, k and the reaction temperature, T, the Arrhenius equation can be considered which is given by [44],

$$ln(k) = -\frac{E_a}{RT} + ln(A), \hspace{2cm} (2.8)$$

where A is the pre-exponential factor, E_a is the activation energy and R is the universal gas constant (8.314 J-mol^{-1} K^{-1}). In general, the Arrhenius equation describes the temperature dependence of the rate constant during a chemical reaction. Considering GNP as the base material, one can use the above relation in order to calculate activation energy involved in GNRs, synthesized at different processing temperatures. By plotting calculated k values in log scale vs. $1/T$, we obtained a trace as depicted in Figure 2.16(b). The activation energy involved in the transformation of nanoparticles (GNP) to nanorods (GNR) mediated via oriented attachment in hydrothermal process can be estimated from the slope and is found as, 25.3 kJ/mol. As predicted earlier, (222) crystallographic plane that corresponded to the most dense (111) plane in the cubic cell can become responsible for the preferential growth owing to minimum surface energy conformation [45]. We anticipate that, the nanorod growth, in the present case, is preceded along the said plane following multi OA events in an organized manner (Figure 2.16(a)).

The room temperature photoluminescence spectra of the synthesized samples (λ_{ex} = 300 nm) are shown in Figure 2.17(a). The spectra of all the samples are characterized by an intense emission located at ~373 nm. This peak can be attributed to the recombination of the delocalized electron close to the conduction band with a single charged state of the surface oxygen vacancy according to the proposition made by Wang et al. and Zhang et al. [21, 46]. The overall luminescence response of the GNRs is found to be less intense with respect to the GNP counterpart. The deconvoluted PL spectra of the GNP and

the GNR (processed at a temperature of 180 °C) are shown in Fig. 6(b) and (c), respectively. Upon deconvolution, an intense defect emission peak can be found at ~405 nm. After assessment of all the spectra, the intensity ratio between ~373 and 405 nm peaks, is observed to be nearly 1.4 times larger in GNRs than that of GNPs. Not surprisingly, it is the defect mediated emission which is mainly responsible for causing asymmetry in the PL spectra. The right symmetry factor (Δ_R/Δ), as defined by the ratio of the wavelength share on the right side of the peak maxima to the full width wavelength at half maxima, is slightly improved with the processing temperature. For GNP, GNR at 140°C and GNR at 180°C, the Symmetry factors were calculated to be 0.55, 0.57 and 0.58 respectively. Furthermore, a high concentration of dislocations and point defects can be anticipated when two particles merged into one eliminating the interface in oriented attachment (OA) process [47]. We invoke that, transformation of particles to nanorods may not necessarily offer new kinds of defects but the latter system is likely to possess ample defect centers that account for adequate recombination events.
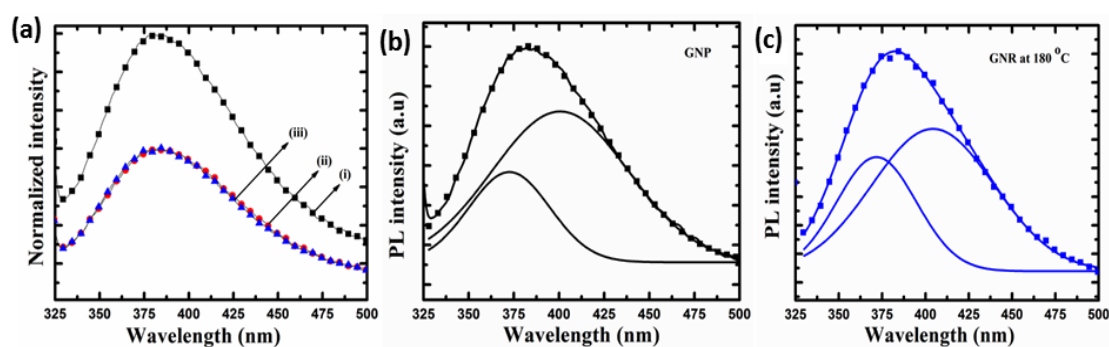

Figure 2.17:(a) PL emission spectra of different Gd$_2$O$_3$ samples: (i) nanoparticles (GNP), and hydrothermally processed nanorods (GNR) at a temperature of (ii) 140 °C and (iii) 180 °C. The deconvoluted PL curves of (b) GNP and (c) GNR systems are shown independently.

Electron paramagnetic resonance (EPR), often referred to as electron spin resonance (ESR), is a widely used spectroscopic technique to study paramagnetic centers in various oxide materials and surfaces [48]. The room temperature, first derivative EPR spectra of the GNP and GNR (processed at

180 °C) systems were recorded in the X-band (9.37 GHz) of the electromagnetic spectrum and with a field modulation of 100 kHz. The variation of signal intensity with the magnetic field is shown in Figure 2.17 .The effective g value was determined from the relation [48]

$$g_{eff} = \frac{hf}{\mu_B H_R} \; , \tag{2.9}$$

where f is the frequency (~9.37 GHz) of the microwave source and μ_B is the Bohr magnetron and H_R is the resonance magnetic field. The effective g value is calculated to be ~2.02, which can account for effective hole trapping in the system ($g>2$) [49]. The respective asymmetry parameters (A/B ratio) for the GNP and GNR systems are ~1.2 and 1. The EPR spectra are isotropic in nature. Though vast number of defect types could influence the EPR spectra drastically, the presence of adequate point defects (say, oxygen vacancies) at the edge boundaries keep the spectra symmetric with no further splitting and additional doublet [50].
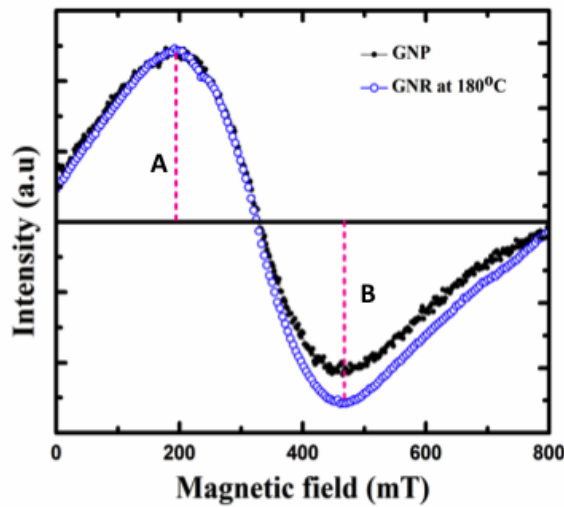

Figure 2.17: Room temperature EPR spectra of the corresponding GNP and GNR systems

2.4 Concluding remarks

A variety of nanosystems have been fabricated considering pure and RE doped form of Gd$_2$O$_3$ system. The optical properties of pure and doped Gd$_2$O$_3$ nanosystems have been explored by analyzing UV-Visible absorption and

photoluminescence spectra. The PL spectra of the Tb³⁺ doped Gd₂O₃ nanoparticles were characterized by *D-F* transition along with various native defect mediated emissions. The surfactant free hydrothermal method is found to be suitable for synthesizing of elongated nanostructure of Gd₂O₃. XRD studies on Gd₂O₃ systems have revealed cubic phase of the as-synthesized nanorods while unsintered Gd(OH)₃ product showed a hexagonal phase. HRTEM analyses have revealed a remarkable distribution of nanoscale rods, with aspect ratio nearly doubled when the precursor used was changed from pH = 10·8 to 13·3. Moreover, the evidence of a clear lattice fringe pattern of the rods and ordered bright spots as observable from SAED, suggests that the samples were highly crystalline in nature. TGA analysis on the hydroxide product has revealed the total weight loss ~ 13·62% up to a temperature of ~ 600 °C. The prominent peak in the Raman spectra attributed to the cubic phase of the nanorods. The magnetic measurements have revealed paramagnetic nature of the Gd₂O₃ nanorods at room temperature. On the other hand, the cubic phase, Gd₂O₃ nanorods were synthesized from nanoparticles via a surfactant free hydrothermal method. Mediated by oriented attachment (OA) mechanism, a complete growth of nanorods was realized when the hydrothermal reaction was carried out at a temperature of 180 °C. The nanorods were expected to have formed through multi-step OA, accompanied with an activation energy of 25 kJ/mol. The EPR spectrum of the nanorods was more isotropic than that of the nanoparticles, while both gave g_{eff} >2.

References

[1] Du, P., Song, Li., Xiong, J., Xi, Z., Jin, D., and Wang, L. Preparation and the luminescent properties of Tb³⁺-doped Gd₂O₃ fluorescent nanofibers via electrospinning. *Nanotechnology,* 22 : 035602(5), 2011.

[2] Hazarika, S., and Mohanta, D. Production and optoelectronic response of Tb³⁺ activated gadolinium oxide nanocrystalline phosphors. *European Physical Journal Applied Physics*, 62: 30401-5, 2013.

[3] Rahman, A.T.M., Vasilev, K., and Majewski, P. Ultra small Gd₂O₃ nanoparticles: Absorption and emission properties. *Journal of Colloid and Interface Science*, 354(2): 592-596, 2011.

[4] Mukherjee, S., Dasgupta, P., and Jana, P. K. Size-dependent dielectric behaviour of magnetic Gd₂O₃ nanocrystals dispersed in a silica matrix. *Journal of Physics D: Applied Physics,* 41: 215004(11p), 2008.

[5] Rogow, D.L., Swanson, C. H., Oliver, A. G., and Oliver, S. R. J. Two related gadolinium aquo carbonate 2-D and 3-D structures and their thermal, spectroscopic, and paramagnetic properties. *Inorganic Chemistry*, 48:1533-41, 2009.

[6]Wood, D.L., and Tauc, J. Weak Absorption Tails in Amorphous Semiconductors. *Physical Review B*, 5: 3144-3151, 1972.

[7] Jia, D., Lu, L., and Yen, W.M. Erbium energy levels relative to the band gap of gadolinium oxide. *Optics Communications*, 212: 97-100, 2002.

[8] Mercier, B., Dujardin, C., Ledoux, G., Louis, C., Tillement, O., and Perriat, P. Observation of the gap blueshift on Gd₂O₃ :Eu³⁺ nanoparticles. *Journal of Applied Physics*, 96: 650-653, 2004.

[9]Dimitrov, V. and Sakka, S. Linear and nonlinear optical properties of simple oxides. II. *Journal of Applied Physics*, 79: 1741-1745, 1996.

[10] Martinet, C., Pillonnet, A., Lancok, J., and Garapon C. Optical, structural and fluorescence properties of nanocrystalline cubic or monoclinic Eu:Lu₂O₃ films prepared by pulsed laser deposition. *Journal of Luminescence*, 126: 807–816,2007.

[11]Dhananjaya, N., Nagabhushana , H., Nagabhushana , B.M., Rudraswamy , B., Sharma , S.C., Sunitha , D.V., Shivakumara , C., and Chakradhar R.P.S. Effect of different fuels on structural, thermo and photoluminescent properties of Gd₂O₃ nanoparticles. *Spectrochimica Acta Part A: Molecular and Biomolecular Spectroscopy*, 96: 532-540, 2012.

[12] Mutelet, B., Perriat, P., Ledoux, G., Amans, D., Lux, F., Tillement, O., Billotey, C., Janier, M., Villiers, C., Bazzi, R., Roux, S., Lu, G., Gong, Q., and Martini. M. Suppression of luminescence quenching at the nanometer scale in Gd₂O₃ doped with Eu³⁺ or Tb³⁺ : Systematic comparison between nanometric and macroscopic samples of life-time, quantum yield, radiative and non-radiative decay rates. *Journal of Applied Physics*, 110: 094317(1-9), 2011.

[13] Stagi, L., Chiriu, D., Ardu, A., Cannas, C., Carbonaro, C. M., and Ricci, P. C. Luminescence enhancement by energy transfer in melamine-Y₂O₃:Tb³⁺ nanohybrids. *Journal of Applied Physics,* 118:125502-7, 2015.

[14] Liu, Y., Yang, P., Wang, W., Dong,H., and Li, Jun. Fabrication and photoluminescence properties of hollow Gd₂O₃:Ln (Ln= Eu³⁺, Sm³⁺) spheres via a sacrificial template method. *Crystal Engineering Communication*, 12: 3717-3723, 2010.

[15] Guo, H., Dong, N., Yin, M., Zhang, W., Lou, L., and Xia, S. Visible upconversion in rare earth ion-doped Gd₂O₃ nanocrystals. *Journal of Physical Chemistry B,* 108 : 19205–19209, 2004.

[16] Thongtem, T., Phuruangrat, A., Ham, D. J., Lee J. S., and Thongtem, S. Controlled Gd₂O₃ nanorods and nanotubes by the annealing of Gd(OH)₃ nanorod and nanotube precursors and self-templates produced by a microwave-assisted hydrothermal process. *Crystal Engineering Communication,* 12: 2962-2966, 2010.

[17]Ningthoujam, R. S., Shukla, R., Vatsa, R. K., Duppel, V., Kienle, L., and Tyagi, A. K. Gd₂O₃:Eu³⁺ particles prepared by glycine- nitrate combustion:

Phase, concentration, annealing, and luminescence studies. *Journal of Applied Physics*, 105: 084304-7, 2009.

[18] Yang, J., Li, C., Cheng, Z., Zhang, X., Quan, Z., Zhang, C., and Lin, J. Size-Tailored Synthesis and Luminescent Properties of One-Dimensional $Gd_2O_3:Eu^{3+}$ Nanorods and Microrods. *Journal of Physical Chemistry C,* 111: 18148-18154, 2007.

[19] Wang, G., Wang, Z., Zhang, Y., Fei, G., and Zhang, L. Controlled synthesis and characterization of large-scale, uniform $Dy(OH)_3$ and Dy_2O_3 single-crystal nanorods by a hydrothermal method. *Nanotechnology,* 15:1307–1311, 2004.

[20]Xu, Z., Yang, Jun., Hou, Z., Li, C., Zhang, C., Huang, S., and Lin, Jun. Hydrothermal synthesis and luminescent properties of $Y_2O_3:Tb^{3+}$ and $Gd_2O_3:Tb^{3+}$ microrods. *Materials Research Bulletin,* 44: 1850–1857, 2009.

[21] Hu,C., Liu, H., Dong, W., Zhang, Y., Bao, G., Lao,C., and Wang, Z. L. $La(OH)_3$ and La_2O_3 nanobelts—synthesis and physical properties. *Advance Materials*, 19: 470–474, 2007.

[22] Pang, M. L., Lin , J., Fu , J., Xing , R.B., Luo , C.X., and Han, Y.C. Preparation, patterning and luminescent properties of nanocrystalline Gd_2O_3: A (A= Eu^{3+}, Dy^{3+}, Sm^{3+}, Er^{3+}) phosphor films via Pechini sol–gel soft lithography. *Optical Materials,* 23: 547–558, 2003.

[23] Kripal, R., and Mishra., I. EPR and optical absorption studies on Gd^{3+} ions in ammonium hydrogen malonate single crystals. *Physica B*, 405: 425–429, 2010.

[24] Rajan, G.,and Gopchandran., K.G. Enhanced luminescence from spontaneously ordered $Gd_2O_3:Eu^{3+}$ based nanostructures. *Applied Surface Science,* 255: 9112-9123, 2009.

[25] Mali, S. S., Betty, C.A., Bhosale,P. N., and Patil, P. S. Hydrothermal synthesis of rutile TiO_2 with hierarchical microspheres and their characterization. *Crystal Engineering Communication,* 13: 6349-6351, 2011.

[26] Clarke, J. and Braginski, A. I. *The SQUID Handbook Vol. I Fundamentals and Technology of SQUIDs and SQUID Systems*. WILEY-VCH Verlag GmbH & Co. KGaA, Weinheim, 2004.

[27] Pascu, O., Carenza, E., Gich, M., Estradé, S., Peiró, F., Herranz, G., and Roig, A. Surface Reactivity of Iron Oxide Nanoparticles by MicrowaveAssisted Synthesis; Comparison with the Thermal Decomposition Route. *The Journal of Physical Chemistry C*, 116: 15108−15116, 2012.

[28] Akdogan, E. K., Rawn, C. J., Porter, W. D., Payzant, E. A., and Safari, A. Size effects in $PbTiO_3$ nanocrystals: effect of particle size on spontaneous polarization and strains. *Journal of Applied Physics*, 97: 084305-8, 2005.

[29] Tong, W., Li, Li., Hu, W., Yan, T., and Li. G. Systematic control of monoclinic $CdWO_4$ nanophase for optimum photocatalytic activity. *Journal of Physical Chemistry C*, 114 : 1512-1519, 2010.

[30] Yang, L., Li, L., Zhao, M., Fu, C., and L. G. Is there lattice contraction in multicomponent metal oxides? Case study for $GdVO_4{:}Eu^{3+}$ nanoparticles. *Nanotechnology* 24: 305701(10pp), 2013.

[31] Nguyen, T. D., Mrabet, D., and Do, T.O. Controlled self-assembly of Sm_2O_3 nanoparticles into nanorods: simple and large scale synthesis using bulk Sm_2O_3 powders. *Journal of Physical Chemistry C*, 112: 15226-15235, 2008.

[32] Lee, K. H., and Byeon S. H. Extended members of the layered rare-earth hydroxide family, $RE_2(OH)_5NO_3{\cdot}nH_2O$ (RE= Sm, Eu, and Gd): Synthesis and anion-exchange behavior. *European Journal of Inorganic Chemistry*, 8: 929-936, 2009.

[33]Wang, X., and Li, Y. Rare-Earth-compound nanowires, nanotubes, and fullerene-like nanoparticles: Synthesis, characterization, and properties. *Chemistry -A European Journal*, 9: 5627-5635, 2003.

[34] Hazarika, S., Paul, N., and Mohanta, D. Rapid hydrothermal route to synthesize cubic-phase gadolinium oxide nanorods. *Bulletin of Materials Science,* 37: 789-796, 2014.

[35] Peng, D. F., Dengfeng Peng, Beysen, S., Li, Q., Jian, J., Sun, Y., and Jiwuer, J. Hydrothermal growth of octahedral Fe_3O_4 crystals. *Particuology,* 7: 35-38, 2009.

[36] Peng, D. F., Beysena, S, , Lia, Q., Suna, Y., Yang, L. Hydrothermal synthesis of monodisperse α-Fe_2O_3 hexagonal platelets. *Particuology* 8: 386-389, 2010.

[37] Mohanta, D., Nath S. S., Mishra N. C., and Choudhury, A. Irradiation induced grain growth and surface emission enhancement of chemically tailored ZnS:Mn/PVOH nanoparticles by Cl^{+9} ion impact. *Bulletin of Materials Science*, 26: 289-294, 2003.

[38] Mohanta, D., Nath, S. S., Bordoloi, A., Choudhury, A., Dolui, S. K., and Mishra, N. C. Optical absorption study of 100-MeV chlorine ion-irradiated hydroxyl-free ZnO semiconductor quantum dots. *Journal of Applied Physics*, 92 : 7149-7152, 2002.

[39] Penn, R. L., and Banfield., J. F. Imperfect oriented attachment: dislocation generation in defect-free nanocrystals. *Science,* 281: 969-971, 1998.

[40] Zhang, J. Huang , F., and Lin, Z. Progress of nanocrystalline growth kinetics based on oriented attachment. *Nanoscale,* 2: 18-34, 2010.

[41] Zhang, Y. X., Guo, Jun., White, T., Tan, T. T. Y., and Xu, R. Y_2O_3:Tb nanocrystals self-assembly into nanorods by oriented attachment mechanism. *Journal of Physical Chemistry C,* 111: 7893-7897, 2007.

[42] Polleux, J.,Pinna, N., Antonietti, M., Niederberger, M. Ligand directed assembly of pre formed titania nanocrystals into highly anisotropic nanostructures. *Advance Materials,* 16: 436-439, 2004.

[43] Tang, Z., Kotov, N. A., and Giersig, M. Spontaneous organization of single CdTe nanoparticles into luminescent nanowires.*Science* , 297: 237-240, 2002.

[44] He, W., and Dickerson, J. H. Thermally driven isotropic crystallinity breaking of nanocrystals: Insight into the assembly of EuS nanoclusters and nanorods with oleate ligands. *Applied Physics Letter*, 98: 081914-3, 2011.

[45]Guo, H., Yang, X. Xiao , T., Zhang, W., Lou , L., and Mugnier, J. Structure and optical properties of sol-gel derived Gd₂O₃ waveguide films. *Applied Surface Science,* 230:215-221, 2004.

[46]Zhang, N., Yi, R., Zhou, L., Gao, G., Shi, R., Qiu, G., and Liu X. Lanthanide hydroxide nanorods and their thermal decomposition to lanthanide oxide nanorods. *Materials Chemistry and Physics*, 114: 160-169, 2009.

[47] Zheng, J. S., Huang, F., Yin, S., Wang, Y., Lin, Z., Wu, X., and Zhao, Y. Correlation between the photoluminescence and oriented attachment growth mechanism of CdS quantum dots. *Journal of American Chemical Society*, 132: 9528-9531, 2010.

[48]Murphy D M. *EPR Spectroscopy of Polycrystalline Oxide Systems I: Metal Oxide Catalysis.* Weinheim: WILEY-VCHVerlag GmbH, 2009.

[49]Howe, R.F., and Gratzel, M. EPR study of hydrated anatase under UV irradiation. *Journal of Physical Chemistry,* 91: 3906-3909, 1987.

[50] Wertz, J. E., Auzins, P., Weeks, R. A., and Silsbee, R. H. Electron spin resonance of F centers in magnesium oxide confirmation of the spin of magnesium-25. *Physical Review,* 107: 1535-1537,1957.